Influence of Phosphate and Silica on U(VI) Precipitation from Acidic and Neutralized Wastewaters

5 AUTHORS, INCLUDING:

Masakazu Kanematsu
Anchor QEA
12 PUBLICATIONS   131 CITATIONS

SEE PROFILE

Nico Perdrial
University of Vermont
32 PUBLICATIONS   224 CITATIONS

SEE PROFILE

Wooyong Um
Pacific Northwest National Laboratory
91 PUBLICATIONS   801 CITATIONS

SEE PROFILE

Jon Chorover
The University of Arizona
250 PUBLICATIONS   4,533 CITATIONS

SEE PROFILE

Environmental Science & Technology

Influence of Phosphate and Silica on U(VI) Precipitation from Acidic and Neutralized Wastewaters

Masakazu Kanematsu,*[†,‡] Nicolas Perdrial,[§,∥] Wooyong Um,[⊥] Jon Chorover,[§] and Peggy A. O'Day[†]

[†]School of Natural Sciences, University of California - Merced, 5200 North Lake Road, Merced, California 95343, United States

[‡]Earth Science Division, Lawrence Berkeley National Laboratory, One Cyclotron Road, Berkeley, California 94720, United States

[§]Department of Soil, Water and Environmental Science, University of Arizona, 1177 E. Fourth St., Tucson, Arizona 85721, United States

[∥]Department of Geology, University of Vermont, 180 Colchester Ave., Burlington, Vermont 05405, United States

[⊥]Energy and Environment Directorate, Pacific Northwest National Laboratory, P7-22, Richland, Washington 99354, United States

S *Supporting Information*

ABSTRACT: Uranium speciation and physical–chemical characteristics were studied in solids precipitated from synthetic acidic to circumneutral wastewaters in the presence and absence of dissolved silica and phosphate to examine thermodynamic and kinetic controls on phase formation. Composition of synthetic wastewater was based on disposal sites 216-U-8 and 216-U-12 Cribs at the Hanford site (WA, USA). In the absence of dissolved silica or phosphate, crystalline or amorphous uranyl oxide hydrates, either compreignacite or meta-schoepite, precipitated at pH 5 or 7 after 30 d of reaction, in agreement with thermodynamic calculations. In the presence of 1 mM dissolved silica representative of groundwater concentrations, amorphous

phases dominated by compreignacite precipitated rapidly at pH 5 or 7 as a metastable phase and formation of poorly crystalline boltwoodite, the thermodynamically stable uranyl silicate phase, was slow. In the presence of phosphate (3 mM), meta-ankoleite initially precipitated as the primary phase at pH 3, 5, or 7 regardless of the presence of 1 mM dissolved silica. Analysis of precipitates by U L$_{III}$-edge extended X-ray absorption fine structure (EXAFS) indicated that "autunite-type" sheets of meta-ankoleite transformed to "phosphuranylite-type" sheets after 30 d of reaction, probably due to Ca substitution in the structure. Low solubility of uranyl phosphate phases limits dissolved U(VI) concentrations but differences in particle size, crystallinity, and precipitate composition vary with pH and base cation concentration, which will influence the thermodynamic and kinetic stability of these phases.
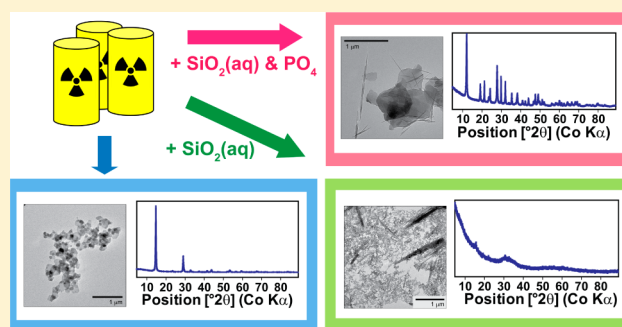
■ INTRODUCTION

Uranium is one of the major contaminants of concern at United States Department of Energy (DOE) legacy high-level radioactive waste sites and is an important contaminant worldwide from mining and milling operations that supported nuclear power generation and former nuclear weapons production. In oxic conditions, uranium is present as uranium(VI) [U(VI)] oxycation, which forms strong aqueous complexes and a variety of solid phases with different ligands.[1,2] Dissolved concentrations of phosphate and silica in aquifer systems, derived from either mineral dissolution or introduced as aqueous species, control the thermodynamic solubility of U(VI) phases and influence kinetic transformations of metastable phases. Thus, amorphous and crystalline U(VI) solids that precipitate from solutions at ambient temperatures over a range of pH may serve as an important sink for U(VI) and control dissolved concentrations in groundwater.

Phosphate reacts with U(VI) to form sparingly soluble U(VI) phosphate phases at acidic-circumneutral pH.[3−5] The presence or absence of phosphate has the potential to determine the assemblage of stable or metastable U(VI) phases. Likewise, the formation of uranyl silicate phases can control dissolved U(VI)

concentrations, but formation of crystalline phases is slow at ambient temperatures and polymeric phases lacking long-range order precipitate initially from solution.[6] In the absence of either phosphate or silica, a variety of more soluble uranyl oxide hydrate phases may form depending on pH, concentrations of base cations, and dissolved uranyl concentrations.[7]

The objectives of this research were to identify and characterize uranyl solid phases that precipitate from simplified acid and neutralized wastewater solutions and to examine the role of dissolved silica and phosphate in the formation of solid phases. Uranium release at the Hanford (Washington, USA) site is used as a real-world guide for experimental design. At the 216-U-8 and U-12 cribs, acidic-circumneutral wastewaters were percolated directly into the vadose zone, and the volume of wastewater discharged was sufficient to cause significant contamination of underlying groundwater and sediment.[8]

66 Acidic wastewater likely reacted with Hanford sediments,
67 resulting in mineral dissolution, transformation, and precip-
68 itation of neo-phases, as has been shown to occur.[9] Here, we
69 compare experimental results and characterizations of pre-
70 cipitated phases with thermodynamic predictions to assess the
71 relative importance of equilibrium versus kinetic constraints on
72 the formation of U(VI) solid phases and dissolved U(VI)
73 concentrations.

■ MATERIALS AND METHODS

75 **Batch Precipitation Experiments.** Triplicate batch experi-
76 ments were conducted using 500 mL volume high-density
77 polyethylene (HDPE) bottles at room temperature (20 °C) in
78 the dark for 30 d (details shown in Figure S1, Supporting
79 Information). Batch experiments were conducted at pH 3, 5,
80 and 7 to span the range of acid neutralization. Estimated
81 chemical compositions of the main waste streams discharged at
82 the Hanford crib sites (Table S1, Supporting Information) were
83 used to design the experimental systems. Solutions (made from
84 ACS grade reagents KNO_3, KCl, $NaNO_3$, and $CaCl_2$)
85 contained ultrapure (Milli-Q) water with 100 mM $[K^+]_T$,
86 1 mM $[Ca^{2+}]_T$, 1 mM $[Na^+]_T$, 100 mM $[NO_3^-]_T$, 1 mM $[Cl^-]_T$
87 with small variations from the addition of trace metal grade acid
88 (HNO_3), base (KOH), and other salts. Solutions were aerated
89 with humidified air for 1 d to equilibrate atmospheric CO_2 at
90 each pH. Dissolved silica and phosphate (added as Na_2SiO_3·
91 $9H_2O$ and KH_2PO_4, respectively) were either absent or added
92 to solutions to achieve a total concentration of 1 mM (for Si)
93 and 3 mM (for P), respectively, the latter based on estimates of
94 waste release at Hanford (Table S1, Supporting Information).
95 The U(VI) stock solution was prepared using $UO_2(NO_3)_2$·
96 $6H_2O$ (Spectrum Chemicals, NJ), and total U(VI) concen-
97 tration was 1 mM in all experiments. After injecting the U(VI)
98 stock solution, pH was slowly increased to the target pH by
99 adding KOH. No buffer was added at pH 3, and MOPS and
100 PIPES were added as buffers to maintain pH at 5.0 and 7.0,
101 respectively. The use of glassware was avoided at all stages of
102 the experiments. Experimental conditions are referred to as
103 follows: 5+U+Si+P: the experiment with solution containing
104 1 mM U(VI), 1 mM dissolved silica, and 3 mM phosphate at
105 pH 5 (Table 1).
106 The batch reactors were placed on an end-over-end shaker at
107 60 rpm. Aliquots of supernatant solutions (3 mL) were
108 collected after U(VI) addition within 15 min, and after 14 and
109 30 d of reaction, filtered through a 0.1 μm PVDF filter unit
110 (Millipore, MA), acidified with HNO_3, and stored at 4 °C until
111 analyses. The suspensions in the batch reactors were
112 centrifuged at 20,000g for 2 h to remove particles ≥25 nm
113 equivalent spherical diameter.[10] The precipitated solids were
114 washed with DI water and recentrifuged three times to remove
115 excess salts. Solids collected from triplicate bottles were
116 combined and homogenized. Air-dried solid yield was 0.2–
117 0.3 g except for 5+U and 5+U+Si where it was 0.05–0.1 g. One
118 of two splits of the wet pastes for specific surface area and bulk
119 chemical analysis was freeze-dried to prevent particle
120 aggregation. The other split was stored as wet-pastes in a
121 refrigerator (4 °C) in the dark and air-dried just before analyses
122 by transmission electron microscopy (TEM), extended X-ray
123 absorption fine structure (EXAFS), and powder X-ray
124 diffraction (XRD). X-ray diffractograms of the U(VI)
125 precipitates were collected twice (after 30 and 210 d of storage
126 at 4 °C as wet pastes) to study effects of wet sample storage on
127 the mineralogy of the U(VI) precipitates. The TEM and

128 EXAFS analyses were conducted after 30 and 180 d of storage
129 at 4 °C as wet pastes, respectively. A set of replicate
130 experiments (7+U+P and 7+U+Si+P) was reacted for 1 d,
131 and the EXAFS spectra were collected for comparison with
132 samples reacted for 30 d. A replicate set (7+U+Si) was also
133 reacted for 30 d, and the precipitate was stored as a wet paste at
134 ambient temperature for 30 d to examine whether storage
135 temperature affected the crystallinity of the precipitate.
136 **Solid Phase Characterization.** Bulk chemical analyses
137 were performed on duplicate digests prepared by dissolving
138 30–50 mg of the freeze-dried U(VI) precipitates in 12 mL of
139 aqua regia (AR, 3 mL of HNO_3 and 9 mL of HCl). Specific
140 surface area (Brunauer–Emmett–Teller (BET), SSA_{BET}) was
141 measured on freeze-dried U(VI) precipitates (Tri-Star 3000,
142 Micrometrics). U(VI) solids were imaged using a JEOL
143 JEM2010 transmission electron microscope (TEM). Thermog-
144 ravimetric analysis (TGA) was carried out to determine the
145 stoichiometric loss of water from U(VI) precipitates by placing
146 a 20 mg sample directly into a platinum crucible under Argon
147 flow (200 mL min^{-1}) and heating at a rate of 2–5 °C min^{-1}
148 from room temperature to 800–1000 °C (Seiko model TGA/
149 DTA 5200). XRD was conducted using a Philips X'pert MPD
150 diffractometer equipped with an ultrafast X'Celerator detector
151 and with a Ni-filtered Co Kα radiation source (λ = 1.78 Å)
152 operated at 50 kV and 40 mA. Samples were mounted on zero-
153 background Si holders and scanned from 4 to 80 degrees 2θ at
154 0.01-degree 2θ steps. Quantitative analysis of X-ray diffracto-
155 grams were performed with the Rietveld module in the X'Pert
156 HighScore Plus software using an internal library of structures
157 extracted from the literature following the method described in
158 Perdrial et al.[11] According to the Highscore Plus Manual,
159 detection limit is 0.5%.
160 Uranium L_{III}-edge X-ray absorption spectra of precipitates
161 and reference compounds were collected on beamline 4−1 at
162 the Stanford Synchrotron Radiation Lightsource (SSRL) under
163 dedicated conditions (current: 450 mA). Details of sample
164 preparation, data collection, processing, and analysis are
165 described in the Supporting Information. Shell-by-shell
166 EXAFS fits were done on the U(VI) reference minerals (total
167 8 minerals, Table S2, Supporting Information) to verify the
168 local bonding around U(VI) based on the crystal structure (see
169 Supporting Information). Unknown precipitates were fit by
170 linear least-squares combinations using the reference U(VI)
171 spectra (k-range: 3−14 Å^{-1}; k^3-weighting). Component weights
172 of the reference spectra were constrained between 0 and 1 in
173 the fit but not forced to sum to unity. Fits were initially
174 performed by trial-and-error using a reference library of the
175 U(VI) reference minerals, and then, the number of reference
176 spectra was restricted on the basis of phases identified by XRD
177 and fit statistics (χ_ν^2 and R-factor as "goodness" of successive
178 fits). Components with a fraction of less than 10% in the fit
179 were removed as they did not significantly improve fit statistics.
180 Phosphuranylite reference compound (synthesized at Wash-
181 ington State University) was analyzed by Raman spectroscopy
182 and synchrotron X-ray diffraction to confirm its identity.
183 **Chemical Analyses.** Dissolved U(VI) concentrations in
184 batch experiments and AR digests were measured using
185 inductively coupled plasma mass spectrometry (ICP-MS)
186 (Agilent Technologies, 7500cs). The method detection limit
187 for U was 50 parts per trillion (ppt). Dissolved Na, K, Ca, P,
188 and Si were measured by the inductively coupled plasma atomic
189 emission spectroscopy (ICP-OES) (PerkinElmer, Optima 5300
190 DV). The method detection limits for Na, K, Ca, P, and Si were

Table 1. Dissolved Concentrations of U, Ca, Si, and P in Precipitation Experiments and Summary of Characterization of Precipitates after 30 d[a]

		log concentration in aqueous phase after 30 d of reaction (mol kg⁻¹)				elemental composition of precipitate (mmol g⁻¹ total solid)[b]						quantitative XRD Rietveld simulations	stoichiometric formula and fractions[f]	SSA$_{BET}$[g] (m²/g)
label	pH	U (log[U]$_{IT}$ = −3.00)	Ca (log[U]$_{IT}$ = −3.00)	Si (log[U]$_{IT}$ = −3.00)	Ca (log[U]$_{IT}$ = −2.52)	U	K	Ca	Si	P	H$_2$O[c]			
(a) 3+U	3	−3.01 (0)	−3.00 (0)			—	—	—	—	—	—	—	—	—
(b) 5+U	5	−4.54 (11)	−3.01 (0)			3.00(0)	0.74(1)	0.02(0)	—	—	4.80	compreignacite	0.83[K$_{1.90}$Ca$_{0.10}$(UO$_2$)$_6$O$_4$(OH)$_6$·8(H$_2$O)] 0.17[(UO$_2$)$_8$O$_2$(OH)$_{12}$·12(H$_2$O)]	0.7 (9)
(c) 7+U	7	−7.61 (1)	−3.02 (0)			3.05(0)	1.03(4)	0.02(0)	—	—	4.80	meta-schoepite	1.00[K$_{1.94}$Ca$_{0.06}$(UO$_2$)$_6$O$_4$(OH)$_6$·8(H$_2$O)]	16.5 (2)
(d) 3+U+Si	3	−3.00 (9)	−3.01 (1)	−3.00 (0)		—	—	—	—	—	—	—	—	—
(e) 5+U+Si	5	−3.19 (0)	−3.02 (0)	−3.08 (1)		3.09(3)	0.74(1)	0.02(0)	0.24(1)	—	5.90	poorly crystalline phases[d] (boltwoodite 62.3%, studtite 31.7%, becquerelite 6.0%)	0.46[K$_2$(UO$_2$)$_2$O$_4$(OH)$_6$·8(H$_2$O)] 0.17[(UO$_2$)$_8$O$_2$(OH)$_{12}$·12(H$_2$O)] 0.17[HK(UO$_2$)(SiO$_4$)·1.5(H$_2$O)] 0.03[Ca(UO$_2$)$_6$O$_4$(OH)$_6$·8(H$_2$O)] 0.17[amorphous SiO$_2$]	3.8 (2)
(f) 7+U+Si	7	−8.46 (16)	−3.02 (0)	−3.37 (0)		2.74(3)	0.96(1)	0.04(0)	0.99(12)	—	6.20	poorly crystalline phases[e] (boltwoodite 100%)	0.27[K$_{1.90}$Ca$_{0.10}$(UO$_2$)$_6$(O$_4$(OH)$_6$·8(H$_2$O)] 0.02[(UO$_2$)$_8$O$_2$(OH)$_{12}$·12(H$_2$O)] 0.22[HK(UO$_2$)(SiO$_4$)·1.5(H$_2$O)] 0.49[amorphous SiO$_2$]	52.7 (5)
(g) 3+U+P	3	−7.24 (1)	−3.00 (0)		−2.72 (1)	2.40(2)	1.59(0)	0.02(0)	—	2.25(0)	4.50	meta-ankoleite	0.43 [K$_2$(UO$_2$)$_2$(PO$_4$)$_2$·5.32(H$_2$O)] 0.57[K$_{5.96}$Ca$_{0.02}$(H$_3$O)$_3$(UO$_2$)$_7$(PO$_4$)$_4$O$_4$·7.09(H$_2$O)]	2.8 (1)
(h) 5+U+P	5	−10.26 (6)	−3.01 (1)		−2.72 (1)	2.40(3)	1.70(2)	0.14(0)	—	2.31(1)	4.90	meta-ankoleite	0.60[K$_2$(UO$_2$)$_2$(PO$_4$)$_2$·5.45(H$_2$O)] 0.36[K$_{5.96}$Ca$_{0.02}$(H$_3$O)$_3$(UO$_2$)$_7$(PO$_4$)$_4$O$_4$·7.27(H$_2$O)] 0.04[Ca$_5$(PO$_4$)$_3$(OH)]	7.0 (1)
(i) 7+U+P	7	−9.66 (3)	−3.30 (3)		−2.77 (1)	2.19(0)	1.50(1)	0.99(1)	—	2.49(1)	5.70	meta-ankoleite	0.41[K$_2$(UO$_2$)$_2$(PO$_4$)$_2$·6(H$_2$O)] 0.32[K$_{5.96}$Ca$_{0.02}$(H$_3$O)$_3$(UO$_2$)$_7$(PO$_4$)$_4$O$_4$·8(H$_2$O)] 0.04[Ca$_5$(PO$_4$)$_3$(OH)]	21.0 (1)
(j) 3+U+Si+P	3	−7.10 (9)	−3.00 (0)	−3.00 (0)	−2.72 (0)	2.48(4)	1.61(2)	0.02(0)	0.0(0)	2.26(0)	4.60	meta-ankoleite	0.38[K$_2$(UO$_2$)$_2$(PO$_4$)$_2$·4.97(H$_2$O)] 0.62[K$_{5.96}$Ca$_{0.02}$(H$_3$O)$_3$(UO$_2$)$_7$(PO$_4$)$_4$O$_4$·6.63(H$_2$O)]	3.0 (1)
(k) 5+U+Si+P	5	−10.07 (1)	−3.03 (1)	−3.00 (0)	−2.71 (0)	2.40(3)	1.58(3)	0.13(0)	0.0(0)	2.17(0)	4.50	meta-ankoleite	0.46[K$_2$(UO$_2$)$_2$(PO$_4$)$_2$·4.98(H$_2$O)] 0.49[K$_{5.96}$Ca$_{0.02}$(H$_3$O)$_3$(UO$_2$)$_7$(PO$_4$)$_4$O$_4$·6.65(H$_2$O)] 0.03[Ca$_5$(PO$_4$)$_3$(OH)]	5.9 (9)
(l) 7+U+Si+P	7	−8.95 (11)	−3.21 (1)	−3.00 (0)	−2.74 (0)	2.39(3)	1.58(2)	0.71(1)	0.0(0)	2.47(6)	4.40	meta-ankoleite	0.28[K$_2$(UO$_2$)$_2$(PO$_4$)$_2$·5.15(H$_2$O)] 0.49[K$_{5.96}$Ca$_{0.02}$(H$_3$O)$_3$(UO$_2$)$_7$(PO$_4$)$_4$O$_4$·6.87(H$_2$O)] 0.23[Ca$_5$(PO$_4$)$_3$(OH)]	24.6 (5)

[a]Elemental analysis, X-ray diffraction, and BET surface area. [b]Stoichiometric formula, elemental composition (mmol/g), and water content (mmol/g) of U reference minerals: compreignacite, K$_2$(UO$_2$)$_6$O$_4$(OH)$_6$·8(H$_2$O) (U: 2.99, K: 0.99, H$_2$O: 5.74); schoepite, (UO$_2$)$_8$O$_2$(OH)$_{12}$·12(H$_2$O) (U: 3.06, H$_2$O: 6.89); meta-schoepite, (UO$_2$)$_4$O(OH)$_6$·5H$_2$O (U: 3.11, H$_2$O: 3.88); studtite, [(UO$_2$)O$_2$(H$_2$O)$_2$](H$_2$O)$_2$ (U: 2.67, H$_2$O: 5.34); becquerelite, Ca(UO$_2$)$_6$O$_4$(OH)$_6$·8(H$_2$O) (U: 3.05, Ca: 0.51, H$_2$O: 5.58); boltwoodite, HK(UO$_2$)(SiO$_4$)·1.5(H$_2$O) (U: 2.33, Si: 2.33, H$_2$O: 4.66); meta-ankoleite, K$_2$(UO$_2$)$_2$(PO$_4$)$_2$·6(H$_2$O) (U: 2.18, K: 2.18, P: 2.18, H$_2$O: 6.55); phosphuranylite, KCa(H$_3$O)$_3$(UO$_2$)$_7$(PO$_4$)$_4$O$_4$·8(H$_2$O) (U: 2.68, K: 0.38, Ca: 0.38, P: 1.53, H$_2$O: 3.06). [c]Determined by TGA analysis. [d]The Rietveld simulation for a sample stored for 210 d: boltwoodite 80.9% + studtite 19.1%. [e]The Rietveld simulation for a sample stored at ambient temp. for 30 d: boltwoodite 100%; a sample stored for 210 d: boltwoodite 100%. [f]Normalized fractions from chemical analysis with phases constrained by XRD and EXAFS. Detailed calculation procedures are described in the Supporting Information. This calculation leaves P (0.39−0.69 mmol·g⁻¹) imbalances. [g]Specific surface area determined by the BET method.
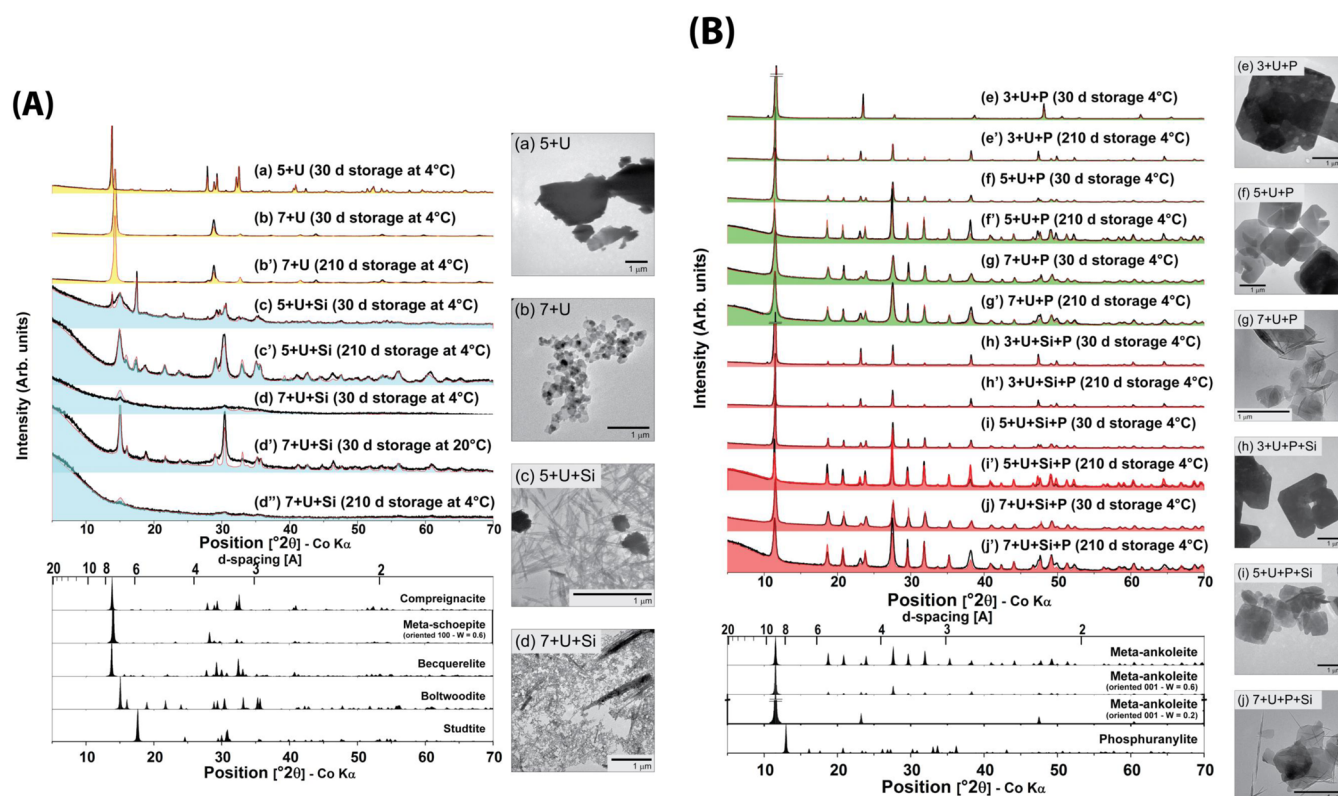
(A)

(B)

Figure 1. X-ray diffractograms (black lines), Rietveld simulated spectrum (colored lines and colored area: yellow for U solids, blue for U+Si solids, green for U+P solids, and red for U+Si+P solids), and TEM images of the U precipitates formed in the absence of phosphate (A) and the presence of phosphate (B). Reference uranyl minerals are shown at the bottom.

24, 20, 10, 10, and 12 ppb, respectively. Dissolved K was not measured because of its high concentration. All standards and samples were analyzed in a 2% HNO_3 matrix for ICP-MS and ICP-OES.

Thermodynamic Modeling. Thermodynamic calculations of the experimental conditions were performed using the software MINEQL+ 4.6[12] and Geochemist's workbench (GWB) 7.0.[13] Calculations were conducted with a modified version of the Lawrence Livermore National Laboratory (LLNL) thermodynamic database thermo.com.v8.r6+[14] with the latest critically reviewed thermodynamic data of stability constants of aqueous U(VI) species[1,15] (Table S3 and S4, Supporting Information) and solubility products (K_{sp}) of U(VI) solids (Table S5, Supporting Information). Activity coefficients were calculated using the Davies equation.

RESULTS

Precipitation Experiments. After injecting the U(VI) stock solution and pH adjustment, yellow and green-yellow precipitates were immediately formed in the absence and presence of phosphate, respectively. No U(VI) solid formed in 3+U and 3+U+Si, where all U(VI) minerals considered were predicted to be undersaturated by thermodynamic calculations as discussed below.

The concentration of dissolved U(VI) immediately decreased after the injection of the U(VI) stock solution and pH adjustment in experiments where visible suspended solids formed (Table 1, Figure S2 and Table S6, Supporting Information). In the absence of phosphate, U(VI) concentrations decreased to 10^{-3}–10^{-8} M after 30 d. In contrast, dissolved U(VI) concentrations rapidly decreased to 10^{-7}–10^{-10} M and remained constant over time in the presence

of phosphate. Dissolved Si concentrations decreased in 5+U+Si (0.83 mM, $10^{-3.08}$ M) and 7+U+Si (0.42 mM, $10^{-3.38}$ M) after 30 d of reaction. In contrast, Si concentrations did not change in 3−7+U+Si+P solids. In the presence of phosphate, dissolved P concentrations immediately decreased to approximately $\sim$2 mM ($10^{-2.7}$ M) after injection of the U(VI) stock solution regardless of the presence of dissolved silica. Dissolved Na concentrations did not change in all experiments (not shown). Decreases in dissolved Ca concentrations were small in most experiments except 7+U+P and 7+U+Si+P, where concentrations gradually decreased to $\sim$0.5 mM ($10^{-3.3}$ M). Dissolved Ca and P concentrations were constant in blank samples.

Solid Phase Characterization. Overall, U(VI) precipitated from different solution compositions was incorporated into solids with covarying mineralogy, chemistry, morphology, particle size, and BET surface area (Table 1, Figure 1). Results of bulk chemical analyses showed K-bearing U solids were dominant in all conditions due to the high K concentrations in the synthetic wastewaters (Table 1). Despite lower initial Ca (1 mM) than K concentrations (100 mM), Ca was detected in the precipitates in variable amounts. Stoichiometric formulas of the precipitates were estimated on the basis of characterization of the solids (described in the Discussion and the Supporting Information). The precipitates formed at higher pH had smaller particle sizes (TEM images, Figure 1) and larger BET surface areas (Table 1).

The X-ray diffractogram of the 5+U solid (Figure 1A (a)) showed distinctive reflection peaks of compreignacite ($K_2(UO_2)_6O_4(OH)_6\cdot 8(H_2O)$), a K-bearing uranyl oxide hydrate. The K content in the 5+U solid was lower than that of compreignacite (Table 1), which may indicate the formation of non K-bearing (amorphous) uranyl

oxide hydrates (e.g., schoepite $((UO_2)_8O_2(OH)_{12}\cdot12(H_2O))$) as secondary phases. The best fit to the XRD of the 7+U solid (Figure 1A (b)) was obtained by oriented-metaschoepite $((UO_2)_4O(OH)_6\cdot5H_2O)$. The XRD of the 7+U solid collected after different storage times (Figure 1A (b) and (b′)) was almost identical, although peak shouldering at 7.4, 3.7, 3.2, and 2.6 Å in the later diffractograms indicated the presence of compreignacite. The stoichiometric formula of the 7+U solid was almost identical to that of compreignacite (Table 1). Small amounts of Ca (0.2 mmol g^{-1}) were detected in the 5+U and 7+U solids, probably due to either Ca substitution for K in the interlayers of the solids or the formation of a small amount of becquerelite $(Ca(UO_2)_6O_4(OH)_6\cdot8(H_2O))$, which was not detected by either XRD or EXAFS (see below).

The 5+U+Si and 7+U+Si solids contained different amounts of Si (0.21 ± 0.01 and 0.99 ± 0.12 mmol g^{-1} total solid, respectively, Table 1), which correspond to stoichiometric U/Si molar ratios 1:0.08 and 1:0.36, respectively. These ratios are much lower than those of uranyl silicates such as soddyite $((UO_2)_2SiO_4\cdot2(H_2O))$ (U/Si molar ratio = 1:1; Si content: 1.50 mmol g^{-1}) and boltwoodite $(HK(UO_2)(SiO_4)\cdot1.5(H_2O))$ (U/Si molar ratio = 1:1; Si content: 2.33 mmol g^{-1}). Therefore, the primary phases formed in 5+U+Si and 7+U+Si by mass were not uranyl silicates but uranyl oxide hydrates. The Rietveld simulation, which is preferential to crystalline phases, showed the presence of mostly boltwoodite, with a lower fraction of studtite $([(UO_2)O_2(H_2O)_2](H_2O)_2)$, a uranyl peroxide, and minor becquerelite in the 5+U+Si solid (Figure 1A (c)). The shape of the peaks suggests that the precipitates were poorly crystalline except for studtite. Partitioning of elemental composition into stoichiometric phases assumed the presence of boltwoodite (all Si), becquerelite (all Ca), compreignacite (excess K), and schoepite (excess U) for hydrated uranyl oxide phases (Table 1 and the Supporting Information). After 210 d of storage (4 °C), the fraction of boltwoodite in the Rietveld simulation increased and was more crystalline, while the studtite fraction decreased and becquerelite was not detected. For the 7+U+Si solid, the XRD at 30 and 210 d (stored at 4 °C) showed broadly oscillating intensities with no distinct reflection peaks (Figure 1A (d) and (d″)). In contrast, distinctive Bragg peaks of boltwoodite appeared in the 7+U+Si solid after 30 d of storage under ambient temperature as wet paste (Figure 1A (d′)). This indicates that storage temperature influenced boltwoodite crystallinity in the 7+U+Si solid. The elemental analysis was partitioned into stoichiometric formulas for compreignacite, schoepite, and boltwoodite based on XRD and EXAFS results (see below and the Supporting Information).

The X-ray diffractograms of all U(VI) solids formed in the presence of phosphate indicated the presence of more or less preferentially oriented meta-ankoleite $(K_2(UO_2)_2(PO_4)_2\cdot6(H_2O))$, a K-bearing uranyl phosphate (Figure 1B). Intensities of the diffraction peaks were weaker at higher pH, indicating the presence of less crystalline U(VI) phases, which is consistent with TEM images. No well-defined reflections from phases other than meta-ankoleite were observed after 210 d of storage. Elemental compositions of the precipitates, however, did not match pure meta-ankoleite and contained different amounts of Ca (0.02–0.99 mmol g^{-1}) depending on pH (Table 1). The Ca contents in the 7+U+P and 7+U+Si solids were much higher than that in other solids and in agreement with lower measured dissolved Ca concentrations (Table 1 and Figure S2, Supporting Information). Silicon was not detected in the solids formed in 3+U+P+Si, 5+U+P+Si, and

7+U+P+Si, in agreement with measured dissolved concentrations (Figure S2, Supporting Information, and Table 1). In 3+U+P and 3+U+Si+P, square and equant particles (∼3 μm) were formed, and particle size was smaller than that of meta-ankoleite (50–300 μm) synthesized by van Haverbeke et al.[16]

Uranium-L$_{III}$ EXAFS. EXAFS spectra of U(VI) reference minerals (total 8 minerals) and their shell-by-shell fitting parameters are discussed in detail in the Supporting Information (Figures S3–5 and Tables S7–11). In general, reference EXAFS spectra were well fit with interatomic distances (Tables S7–11, Supporting Information) from their crystal structures reported in the literature (Figures S6–12, Supporting Information).

EXAFS spectra of the precipitates were well fit using linear combinations of either one or two reference spectra. Linear combination fits (LCF) showed that compreignacite dominated the EXAFS spectra of 5+U and 7+U solids (Figure 2 and Table 2) and contributions of other phases were statistically insignificant. The EXAFS spectra of the 5+U+Si and 7+U+Si solids were also similar to that of compreignacite, and LCF indicated compreignacite and small amounts of schoepite (10 and 18%) were the dominant U-bearing phases (Table 2).

The EXAFS spectra of the U(VI) solids formed in the presence of phosphate were quite different from that of meta-ankoleite ("autunite-group"), although the X-ray diffractograms of those solids indicated meta-ankoleite as a dominant phase. Their EXAFS spectra were reproduced with a combination of meta-ankoleite and phosphuranylite $[KCa(H_3O)_3(UO_2)_7(PO_4)_4O_4\cdot8(H_2O)]$ in different proportions but dominated by phosphuranylite. Phosphuranylite belongs to the phosphuranylite group, which is another major group of uranyl phosphates.[3,17] EXAFS spectra of 7+U+P and 7+U+Si+P solids were collected after 1 d of reaction in a replicate experiment (Figure 2B). Spectra of these solids were similar to that of meta-ankoleite in LCF (Figure 2), and interatomic distances determined in shell-by-shell fits of the precipitate spectra matched the local oxygen bonding environment of U(VI) in meta-ankoleite (Table S12 and Figure S13, Supporting Information).

Thermodynamic Calculations. Thermodynamic solubility of U(VI) minerals is displayed as a function of pH together with the experimentally determined dissolved U concentrations after 30 d of reaction ($U_{diss-exp}$) (Figure 3). Compreignacite has the lowest solubility in the absence of dissolved silica and phosphate, followed by schoepite, at pH 5–7 (Figure 3A). Schoepite solubility is similar to that of compreignacite at pH 5. Calculated dissolved U(VI) concentrations at equilibrium ($U_{diss-equil}$) agreed with observed concentrations ($U_{diss-exp}$) at pH 3 (undersaturated with respect to all U(VI) oxide hydrates) and 5. $U_{diss-exp}$ was slightly lower than $U_{diss-equil}$ at pH 7. In the presence of dissolved Si, boltwoodite has the lowest equilibrium solubility at pH 5–7, followed by uranophane $(Ca(UO_2)_2(SiO_3OH)_2\cdot5H_2O)$, compreignacite, and soddyite (Figure 3B). At pH 5 and 7, $U_{diss-exp}$ was higher than $U_{diss-equil}$ in equilibrium with boltwoodite, indicating the systems did not reach equilibrium after 30 d of reaction. In the presence of phosphate, meta-ankoleite is the most thermodynamically stable phase, followed by autunite $(Ca(UO_2)_2(PO_4)_2\cdot10-12(H_2O))$; reliable thermodynamic data have not been reported for phosphuranylite solubility. The reliability of the published solubility product (K_{sp}) of meta-ankoleite used here is somewhat equivocal due to lack of (1) solid phase characterization before and after the experiment to ensure stability of the mineral, (2) attainment of equilibrium from both undersaturated and supersaturated states, and (3) measurement of pH and all dissolved
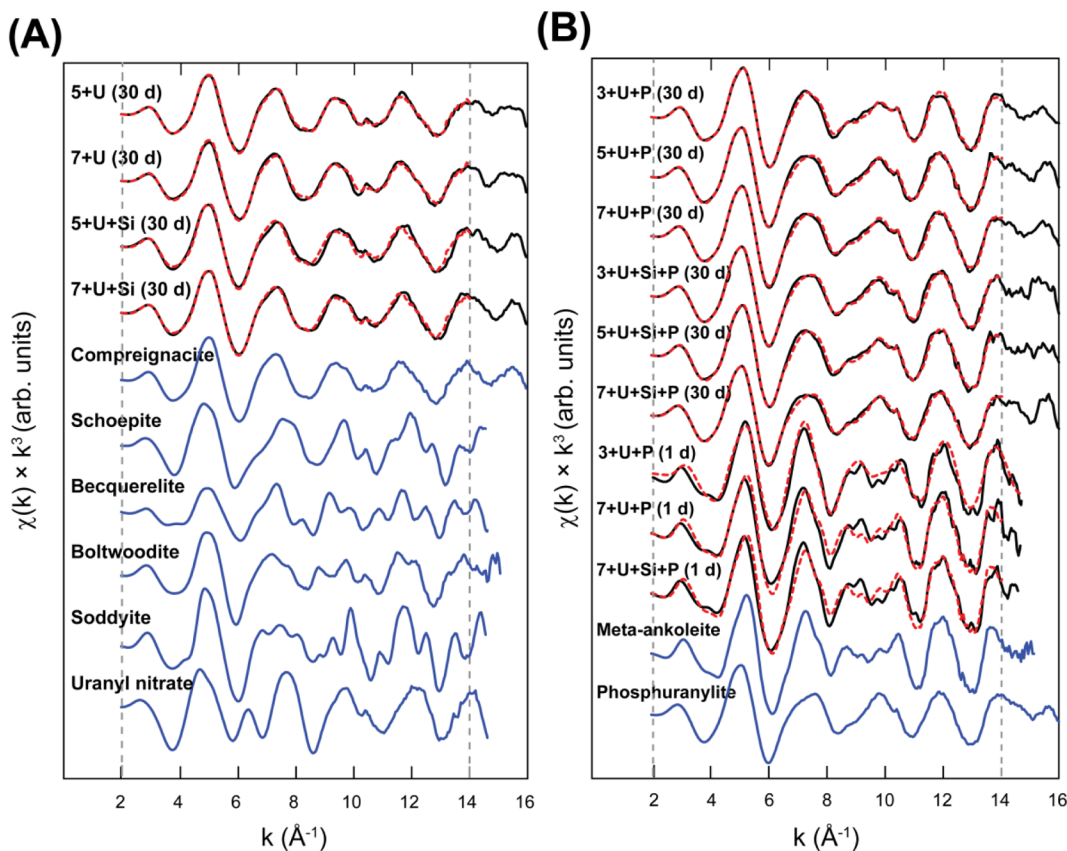
Figure 2. Linear combination fits (red dashed lines) to the EXAFS spectra (black solid lines) of U solids formed (A) in the absence of phosphate (5+U, 7+U, 5+U+Si, and 7+U+Si) and (B) in the presence of phosphate (3+U+P, 5+U+P, 7+U+P, 3+U+Si+P, 5+U+Si+P, and 7+U+Si+P). Uranium reference compounds (blue lines) used as standards are shown at the bottom. Linear combination fits were performed in k-space from 2 to 14 $Å^{-1}$. "30 d" and "1 d" indicate reaction times in batch reactors. Fit results are given in Table 2.

Table 2. Uranium L_{III}-Edge EXAFS Linear-Combination Fit (LCF) Results for Solids

sample[a]	standards[b]				component sum	χ_ν^{2c}	R-factor[d]
	schoepite	compreignacite	meta-ankoleite	phosphuranylite			
(a) 5+U	−	0.92(0)	−	−	0.92	0.08	0.005
(b) 7+U	−	0.94(2)	−	−	0.94	0.04	0.017
(c) 5+U+Si	0.18(1)	0.79(2)	−	−	0.97	0.05	0.018
(d) 7+U+Si	0.10(1)	0.93(1)	−	−	1.03	0.04	0.015
(e) 3+U+P	−	−	0.34(1)	0.68(1)	1.02	0.05	0.013
(f) 5+U+P	−	−	0.14(2)	0.86(2)	1.00	0.14	0.034
(g) 3+U+P	−	−	0.20(1)	0.80(2)	1.00	0.12	0.032
(h) 3+U+Si+P	−	−	0.15(2)	0.85(2)	1.99	0.10	0.027
(i) 5+U+Si+P	−	−	0.30(2)	0.71(2)	1.01	0.14	0.035
(j) 7+U+Si+P	−	−	0.10(2)	0.89(2)	0.99	0.12	0.033
(g′) 7+U+P (air-dried after 1 d)	−	−	1.00(0)	0.00(0)	1.00	0.44	0.083
(j′) 7+U+Si+P (air-dried after 1 d)	−	−	1.00(0)	0.00(0)	1.00	0.46	0.082

[a]All samples reacted for 30 d except for (g′) and (f′) which were reacted for 1 d. [b]Components that did not contribute more than 10% to the total EXAFS fit were eliminated from the final LCF; see the Supporting Information for analysis of all reference compounds. [c]χ_ν^2 is a reduced least-squares goodness-of-fit parameter (=(F-factor)/(# of points − # of variables)). [d]R-factor is a measure of closeness of fit (=$\Sigma((data_i) - (fit_i))^2/\Sigma(data_i)^2$).

ions at equilibrium conditions (Table S5, Supporting Information).[2] This uncertainty may explain the discrepancies between $U_{diss-exp}$ and $U_{diss-equil}$ at pH 3 and 5 in Figure 3C,D. Uranyl carbonates were predicted to be undersaturated at pH less than 7 (Figure S14, Supporting Information), and they were also not detected by XRD or EXAFS.

To predict effects of variable dissolved concentrations and pH on stability of uranyl solids, equilibrium U(VI) solid phases at total U(VI) activity ($a_{U(VI)}$) of 10^{-3} M are displayed as a

function of log activity of K^+ (log (a_{K+})) and log activity of dissolved silica (log (a_{SiO_2})) in the absence of phosphate (Figure 4A) and as a function of log activity of K^+ (log (a_{K+})) and log activity of phosphate (log (a_{PO_4})) in the presence of phosphate (Figure 4B) at pH 5 and 7. Thermodynamic calculations show that U(VI) solid phases predicted to occur in equilibrium with constant U(VI) concentrations (=10^{-3} M) in the absence of phosphate were (meta-) schoepite, compreignacite,
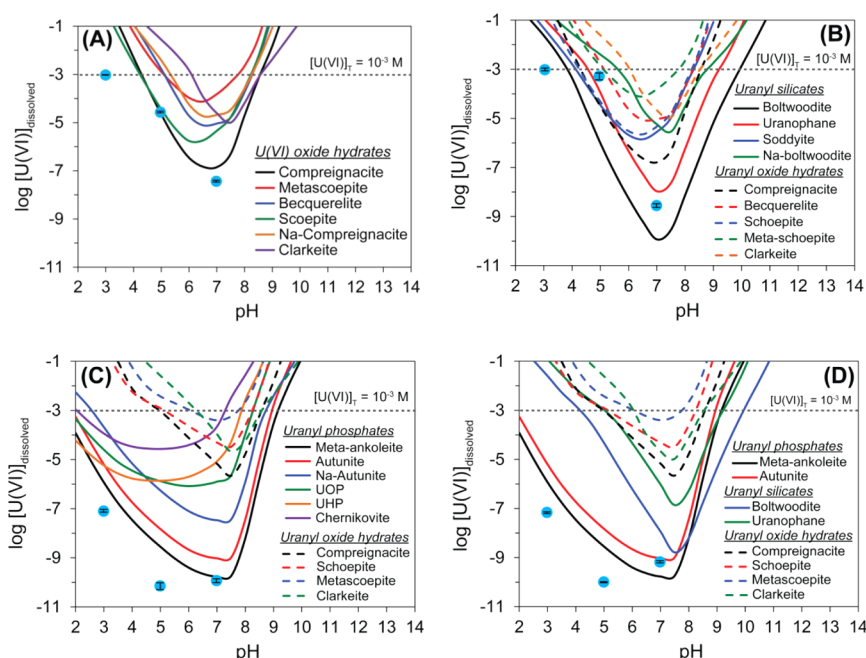
Figure 3. Equilibrium solubility of U minerals (colored lines) in synthetic wastewaters ($[U(VI)]_T = 10^{-3}$ M, $[K]_T = 10^{-1}$ M, $[Na]_T = 10^{-3}$ M, $[Ca]_T = 10^{-3}$ M, $[NO_3^-] \approx 10^{-1}$ M) as a function of log $[U(VI)]$ dissolved concentration and pH with experimentally determined dissolved U concentrations (blue solid dots; error bar is the analytical standard deviation): (A) in the absence of dissolved Si and P (3+U, 5+U, and 7+U), (B) in the presence of dissolved Si ($[SiO_2]_T = 10^{-3}$ M) (3+U+Si, 5+U+Si, and 7+U+Si), (C) in the presence of phosphate ($[PO_4]_T = 3 \times 10^{-3}$ M) (3+U+P, 5+U+P, and 7+U+P), and (D) in the presence of dissolved Si and phosphate ($[SiO_2]_T = 10^{-3}$ M, $[PO_4]_T = 3 \times 10^{-3}$ M) (3+U+Si+P, 5+U+Si+P, and 7+U+Si+P).

395 boltwoodite, and uranophane. As phosphate concentration
396 increases, meta-ankoleite and autunite replace boltwoodite and
397 uranophane as the thermodynamically stable U(VI) phases. The
398 same stability diagrams as Figure 4 at different total U(VI)
399 activities are presented and discussed in the Supporting
400 Information to show changes in solid phase stability fields with
401 U(VI) concentration (Figure S15, Supporting Information).

■ DISCUSSION

402
403 **Uranium Solids in the Absence of Dissolved**
404 **Phosphate.** In systems without dissolved silica and phosphate,
405 characterizations indicate that the primary phase formed at pH
406 5 (5+U) was compreignacite, consistent with thermodynamic
407 calculations. Compreignacite is known as a secondary uranyl
408 phase in the oxidative corrosion of synthetic $UO_2(s)$.[18−20] To
409 account for K in the 5+U solid lower than stoichiometric K in
410 compreignacite, schoepite was assumed to be an additional
411 phase together with a partially $K^+ \Leftrightarrow Ca^{2+}$ exchanged
412 compreignacite (Table 1). In the 7+U solid, EXAFS and bulk
413 chemical analysis indicated that the primary phase was
414 compreignacite. The EXAFS spectrum of compreignacite is
415 distinct from those of schoepite[21] and meta-schoepite,[22] which
416 did not fit the precipitate spectrum. Although the Rietveld
417 simulation showed that the best fit for the 7+U solid was
418 obtained with oriented meta-schoepite, the X-ray diffractogram
419 can also be fit by compreignacite with a slight change in
420 structural parameters (a: 7.16 → 7.20 Å; b: 14.84 → 14.74 Å;
421 c: 12.17 → 12.32 Å). Small particle size, strong preferred
422 orientation, and broad peaks suggest that the precipitates have
423 low crystallinity, which can accommodate compositional
424 variations. Therefore, the results collectively indicate that
425 compreignacite was the primary phase in the 7+U solid.

426 The primary phase formed in the presence of 1 mM
427 dissolved Si (5+U+Si and 7+U+Si) was amorphous com-
428 preignacite, which had no well-defined reflections in XRD
429 (Figure 1A (c−d″)). Compreignacite formed rapidly with
430 short-range order, as indicated by its dominance of EXAFS
431 spectra, but it did not develop long-range ordering to produce
432 reflections in XRD, even after 30 d of reaction and 210 d of
433 storage at 4 °C. As proposed in another study,[23] we suggest that
434 small amounts of water contained within nanopores have been
435 subjected to radiolysis during storage, generating enough H_2O_2
436 to form small amounts of metastable studtite. The stoichio-
437 metric formulas of the 5+U+Si and 7+U+Si solids can be
438 assigned assuming compreignacite is the dominant U phase.
439 The fractions of boltwoodite and other phases (becquerelite,
440 hydrated uranyl oxides as schoepite, and amorphous SiO_2) were
441 determined from the total Si, Ca, and K measured in the solids
442 (Table 1). According to estimated stoichiometric formulas, U
443 mass fractions of boltwoodite from analysis of XRD were 4%
444 and 11% U in the 5+U+Si and 7+U+Si solids, respectively,
445 corresponding to molar ratios of 17% and 22% in Table 1.
446 Boltwoodite was not identified as an important phase in the
447 EXAFS LCF (Table 2) because its contribution was smaller
448 than 10% in the fit. Because X-ray absorption is element specific
449 and proportional to molar absorption, spectra composed of
450 mixtures will be biased toward those phases with higher
451 stoichiometric amounts of U (e.g., compreignacite with 6 U
452 versus boltwoodite with 1 U per formula unit) compared to
453 XRD, which is sensitive to long-range order within the solid
454 phase. In samples stored for 210 d at 4 °C and 30 d at 20 °C,
455 boltwoodite developed sufficient long-range ordering to produce
456 reflections with variable amplitude in XRD (Figure 1A (c), (c′),
457 and (d′); samples not analyzed by EXAFS). This indicates that

(A) $(UO_2^{2+})_T = 10^{-3}$ M
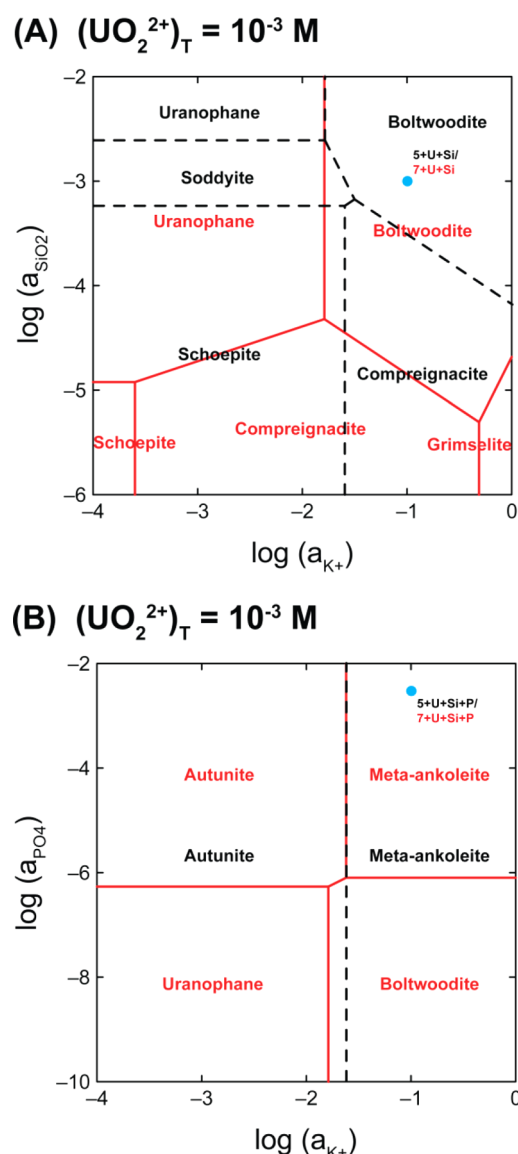

(B) $(UO_2^{2+})_T = 10^{-3}$ M

Figure 4. Stability diagrams depicting equilibrium U(VI) phases at pH 5 (dashed black lines) and pH 7 (solid red lines) as a function of (A) log activity of K$^+$ (log (a_{K^+})) and log activity of SiO$_2$ (log (a_{SiO_2})) in the absence of phosphate and (B) log activity of K$^+$ (log (a_{K^+})) and log activity of phosphate (log (a_{PO_4})) in the presence of phosphate. In both systems, (U(VI))$_T$ = 10^{-3}, (Ca^{2+})$_T$ = 10^{-3}, (Na+)$_T$ = 10^{-3}, (NO$_3^-$)$_T$ = 10^{-3}, and (Cl$^-$)$_T$ = 10^{-3}. Blue solid points represent the initial experimental conditions.

458 temperature,[6] aging time, and pH profoundly influence the
459 development of long-range structure in boltwoodite.
460   The experimental results and thermodynamic calculations
461 (Figure 3B) indicate that suspensions reached equilibrium with
462 respect to compreignacite and several other uranyl oxide
463 hydrates, but not boltwoodite, after 30 d of reaction. These
464 observations emphasize the importance of polymerization and
465 solid-state transformation rates of uranyl silicate phases. For
466 example, Wronkiewicz et al.[19] reported that unirradiated
467 UO$_2$(s) pellet initially altered to uranyl oxide hydrates in contact
468 with oxic groundwater containing dissolved Si (1.61 mM as SiO$_2$)
469 and that uranyl silicates formed over longer contact times (>6 yr).
470 Gorman-Lewis et al.[24] reported that 6 weeks of aging at ambient
471 temperature were required for amorphous uranyl silicate phases to

472 rearrange and develop midrange structural linkages characteristic
473 of crystalline phases. Therefore, uranyl silicate phases such as
474 boltwoodite may form and develop long-range structure in the
475 presence of dissolved Si at the expense of uranyl oxide hydrate
476 phases such as compreignacite. The presence of Si may also
477 contribute to the slow transformation of amorphous compreigna-
478 cite to a more crystalline phase.
   Uranium Solids in the Presence of Dissolved
479 **Phosphate.** In the presence of phosphate, meta-ankoleite
480 was the initial phase formed under all conditions according to
481 XRD and EXAFS spectra of U(VI) precipitates aged for 1 d.
482 Thermodynamic calculations also show that meta-ankoleite is
483 the most stable phase in the presence of phosphate (given
484 available thermodynamic data). After 30 d of reaction,
485 "autunite-type" uranyl phosphate sheets of meta-ankoleite
486 were transformed mostly to "phosphuranylite-type" sheets
487 based on LCF of EXAFS spectra (67−89% phosphuranylite).
488 Catalano and Brown[25] showed that the EXAFS spectrum of
489 meta-autunite (Ca(UO$_2$)$_2$(PO$_4$)$_2$·6(H$_2$O)), the Ca endmember
490 of a solid-solution with meta-ankoleite, is nearly identical to
491 that of meta-ankoleite, while the spectrum of phosphuranylite is
492 distinctly different. The absence of reflection peaks of
493 phosphuranylite in XRD of the precipitates (Figure 1B)
494 indicates that this phase lacked long-range structure. The
495 phosphuranylite reference compound used in EXAFS fits was
496 amorphous in synchrotron-XRD (Figure S16, Supporting
497 Information), but its identity was confirmed by Raman
498 spectroscopy (Figure S17, Supporting Information) and by
499 shell-by-shell fitting of the EXAFS spectrum and comparison
500 with interatomic distances derived from crystal structure
501 determinations (Figure S5 and Table S6, Supporting
502 Information). The bulk chemical composition of the precip-
503 itates with phosphate was partitioned among meta-ankoleite,
504 phosphuranylite (K$_2$Ca(UO$_2$)$_7$(PO$_4$)$_4$(OH)$_6$·6H$_2$O, also known
505 as yingjiangite[26]), and hydroxyapatite (Ca$_5$(PO$_4$)$_3$(OH)) assum-
506 ing: (1) the fraction of meta-ankoleite and phosphuranylite
507 (73−86%) should be close to the values determined by EXAFS
508 (67−89%) and (2) excess Ca and PO$_4$ is assigned to hydro-
509 xyapatite (see details in the Supporting Information; Table 1).
510 This calculation leaves an excess of 0.39−0.69 mmol g^{-1}
511 phosphate, which may be trapped into the solids as H$_3$PO$_4^0$
512 during the transformation of uranyl phosphate sheets.
513   The presence of Ca^{2+} likely induced the transformation of
514 meta-ankoleite to phosphuranylite even though its initial
515 concentration in solution (1 mM) was 100 times lower than
516 the K$^+$ concentration (100 mM). The autunite group contains
517 highly symmetric uranyl phosphate sheets formed by uranyl
518 square bipyramids that corner-share with phosphate tetrahedra
519 (Figure S11, Supporting Information). In contrast, the
520 "phosphuranylite-type" sheet is composed of hexagonal,
521 pentagonal, and tetragonal uranyl bipyramids linked through
522 phosphate tetrahedra (Figure S12, Supporting Information).
523 Different stoichiometries for phosphuranylite have been
524 reported and indicate that the molar ratio of K to Ca may
525 vary from one.[27,28] The transformation from meta-ankoleite to
526 phosphuranylite may be responsible for dissolved U(VI)
527 concentrations lower than predicted by equilibrium with
528 meta-ankoleite (Figure 3C,D), although the U(VI) solubility
529 of phosphuranylite has not been well established thermody-
530 namically. Phosphuranylite is often associated with autunite
531 group minerals such as autunite and meta-ankoleite.[27] For
532 example, Morris et al.[29] reported that variable mixtures of meta-
533 autunite, phosphuranylite, and uranyl hydroxide (schoepite)

were the primary U(VI) phases in contaminated soils and sediments at the U.S. DOE Fernald site.

Implications for Subsurface Systems. The results emphasize the importance of amorphous and thermodynamically metastable phases, particle size, and crystallinity, in controlling dissolved U(VI) concentrations in sediments impacted by acidic-circumneutral U(VI) waste discharges. Although the systems studied here are simplified relative to reactions in the vadose zone,[30,31] they point out the importance of dissolved phosphate in precipitation of solids even in the presence of dissolved silica, which had no apparent effect on reaction products. Crystalline and amorphous uranyl phosphate phases (meta-ankoleite, phosphuranylite) precipitated rapidly from solutions at acidic to circumneutral pH. If these types of phases precipitate in the vadose zone, their low thermodynamic solubility will limit dissolved U(VI) concentrations in groundwater. The concentrations of base cations, particularly K^+ and Ca^{2+}, will determine the composition and structure of the uranyl phosphate phase. The conversion of an autunite-type phase (meta-ankoleite) to an amorphous phosphuranylite-type phase observed between 1 and 30 d of reaction in solutions with 100 times higher K^+ than Ca^{2+} concentration demonstrates the disproportionate influence of divalent Ca as a structure-determining ion. Thus, the concentration of Ca^{2+} (and other divalent cations) relative to monovalent cations in groundwater will exert an important control on the type and stability of uranyl phosphate phases.

In the absence of either silica or phosphate, formation of crystalline or amorphous uranyl oxide hydrates, either compreignacite or meta-schoepite, was consistent with thermodynamic calculations. The equilibrium solubility of these phases is orders-of-magnitude higher than that of uranyl phosphate phases. With the addition of dissolved silica, amorphous compreignacite (±minor meta-schoepite) precipitated rapidly as a metastable phase and formation of boltwoodite, the thermodynamically stable uranyl silicate phase, was slow. In acid-impacted sediments in the vadose zone such as those at the Hanford site, dissolved silica concentrations will vary with the extent of reaction of silicate minerals and acid neutralization. Dissolved U(VI) concentrations at equilibrium will vary by ~2−3 orders of magnitude depending on the amount of U(VI) bound in less soluble, neoformed uranyl silicate minerals (e.g., boltwoodite) compared to more soluble uranyl oxide hydrates (compreignacite or meta-schoepite). Furthermore, at higher pH in the presence of dissolved silica, compreignacite was observed to precipitate with smaller particle size and lower crystallinity, which will likely enhance dissolution rates. Mobilization of U from sediments can be simulated quantitatively using reactive transport models with knowledge of the identity of crystalline or amorphous U-bearing phases and consideration of the thermodynamic solubility and kinetic stability of these phases.

■ ASSOCIATED CONTENT

Ⓢ Supporting Information

Detailed information about composition of the waste streams discharged to 216-U-8 and U-12 at the Hanford site, details of experimental methods and analyses, thermodynamic constants, EXAFS fits of reference compounds, additional solubility diagrams, characterization of the phosphuranylite reference compound, and procedures to determine stoichiometric formula of the precipitates. This material is available free of charge via the Internet at http://pubs.acs.org.

■ AUTHOR INFORMATION

Corresponding Author
*E-mail: mkanematsu@lbl.gov.

Notes
The authors declare no competing financial interest.

■ REFERENCES

(1) Guillaumont, R.; Fanghänel, T.; Fuger, J.; Grenthe, I.; Neck, V.; Palmer, D. A.; Rand, M. H. *Update on the Chemical Thermodynamics of Uranium, Neptunium, Plutonium, Americium and Technetium.* Elsevier: Amsterdam, 2003.

(2) Gorman-Lewis, D.; Burns, P. C.; Fein, J. B. Review of uranium mineral solubility measurements. *J. Chem. Thermodyn.* **2008**, *40* (3), 335−352.

(3) Burns, P. C. The crystal chemistry of uranium. In *Uranium: Mineralogy, Geochemistry and the Environment*; Burns, P. C.; Finch, R., Eds.; Mineralogical Society of America: Washington, DC, 1999; pp 23−90.

(4) Gorman-Lewis, D.; Shvareva, T.; Kubatko, K.; Burns, P. C.; Wellman, D. M.; McNamara, B.; Szymanowski, J. E. S.; Navrotsky, A.; Fein, J. B. Thermodynamic properties of autunite, uranyl hydrogen phosphate, and uranyl orthophosphate from solubility and calorimetric measurements. *Environ. Sci. Technol.* **2009**, *43* (19), 7416−7422.

(5) Wellman, D. M.; Gunderson, K. M.; Icenhower, J. P.; Forrester, S. W. Dissolution kinetics of synthetic and natural meta-autunite minerals, $X_{3-n}^{(n)+}[(UO_2)(PO_4)_2] \cdot xH_2O$, under acidic conditions. *Geochem., Geophys., Geosyst.* **2007**, *8*; DOI: 10.1029/2007GC001695.

(6) Soderholm, L.; Skanthakumar, S.; Gorman-Lewis, D.; Jensen, M. P.; Nagy, K. L. Characterizing solution and solid-phase amorphous uranyl silicates. *Geochim. Cosmochim. Acta* **2008**, *72* (1), 140−150.

(7) Gorman-Lewis, D.; Fein, J. B.; Burns, P. C.; Szymanowski, J. E. S.; Converse, J. Solubility measurements of the uranyl oxide hydrate phases metaschoepite, compreignacite, Na-compreignacite, becquerelite, and clarkeite. *J. Chem. Thermodyn.* **2008**, *40* (6), 980−990.

(8) Williams, B. A.; Chou, C. J. *Interim-Status Groundwater Quality Assessment Plan for the 216-U-12 Crib*; Westinghouse Hanford Company: Richland, WA, 1993.

(9) Gunter, W. D.; Perkins, E. H.; Hutcheon, I. Aquifer disposal of acid gases: Modelling of water-rock reactions for trapping of acid wastes. *Appl. Geochem.* **2000**, *15* (8), 1085−1095.

(10) Gimbert, L. J.; Haygarth, P. M.; Beckett, R.; Worsfold, P. J. Comparison of centrifugation and filtration techniques for the size fractionation of colloidal material in soil suspensions using sedimentation field-flow fractionation. *Environ. Sci. Technol.* **2005**, *39* (6), 1731−1735.

(11) Perdrial, N.; Rivera, N.; Thompson, A.; O'Day, P. A.; Chorover, J. Trace contaminant concentration affects mineral transformation and pollutant fate in hydroxide-weathered Hanford sediments. *J. Hazard. Mater.* **2011**, *197*.

(12) Schecher, W. D.; McAvoy, D. C. *MINEQL+: A Chemical Equilibrium Modeling System, Version 4.6*; Environmental Research Software: Hallowell, ME, 2007.

(13) Bethke, C. M. *The Geochemist's Workbench, Version 7.0*; Hydrogeology Program, University of Illinois: Urbana, 2007.

(14) Delany, J. M., Lundeen, S. R. The LLNL thermochemical database. In *Lawrence Livermore National Laboratory Report, UCRL-21658*; Lawrence Livermore National Laboratory: Livermore, CA, 1990; p 150.

(15) Dong, W.; Brooks, S. C. Determination of the formation constants of ternary complexes of uranyl and carbonate with alkaline earth metals (Mg^{2+}, Ca^{2+}, Sr^{2+}, and Ba^{2+}) using anion exchange method. *Environ. Sci. Technol.* **2006**, *40* (15), 4689−4695.

(16) VanHaverbeke, L.; Vochten, R.; VanSpringel, K. Solubility and spectrochemical characteristics of synthetic chernikovite and meta-ankoleite. *Mineral. Mag.* **1996**, *60* (402), 759−766.

(17) Finch, R.; Murakami, T. Systematics and paragenesis of uranium minerals. In *Uranium Mineralogy, Geochemistry and the Environment*; Burns, P. C.; Finch, R., Eds.; Mineralogical Society of America: Washington, DC, 1999; pp 91−179.

(18) Elton, N. J.; Hooper, J. J.; Ryback, G. Compreignacite - A 2nd occurrence, from St. Just, Cornwall. *Mineral. Mag.* **1994**, *58* (391), 339−341.

(19) Wronkiewicz, D. J.; Bates, J. K.; Wolf, S. F.; Buck, E. C. Ten-year results from unsaturated drip tests with UO_2 at 90°C: Implications for the corrosion of spent nuclear fuel. *J. Nucl. Mater.* **1996**, *238* (1), 78−95.

(20) Burns, B. C. The structure of compreignacite, $K_2[(UO_2)_3O_2(OH)_3]_2 \cdot 7(H_2O)$. *Can. Mineral.* **1998**, *36*, 1061−1067.

(21) Allen, P. G.; Shuh, D. K.; Bucher, J. J.; Edelstein, N. M.; Palmer, C. E. A.; Silva, R. J.; Nguyen, S. N.; Marquez, L. N.; Hudson, E. A. Determinations of uranium structures by EXAFS: Schoepite and other U(VI) oxide precipitates. *Radiochim. Acta* **1996**, *75* (1), 47−53.

(22) Froideval, A.; Del Nero, M.; Gaillard, C.; Barillon, R.; Rossini, I.; Hazemann, J. L. Uranyl sorption species at low coverage on Al-hydroxide: TRLFS and XAFS studies. *Geochim. Cosmochim. Acta* **2006**, *70* (21), 5270−5284.

(23) Eriksen, T. E.; Shoesmith, D. W.; Jonsson, M. Radiation induced dissolution of UO2 based nuclear fuel - A critical review of predictive modelling approaches. *J. Nucl. Mater.* **2012**, *420* (1−3), 409−423.

(24) Gorman-Lewis, D.; Skanthakumar, S.; Jensen, M. P.; Mekki, S.; Nagy, K. L.; Soderholm, L. FTIR characterization of amorphous uranyl-silicates. *Chem. Geol.* **2008**, *253* (3−4), 136−140.

(25) Catalano, J. G.; Brown, G. E. Analysis of uranyl-bearing phases by EXAFS spectroscopy: Interferences, multiple scattering, accuracy of structural parameters, and spectral differences. *Am. Mineral.* **2004**, *89* (7), 1004−1021.

(26) Frost, R. L.; Cejka, J.; Ayoko, G. Raman spectroscopic study of the uranyl phosphate minerals phosphuranylite and yingjiangite. *J. Raman Spectrosc.* **2008**, *39* (4), 495−502.

(27) Frondel, C. Studies of uranium minerals (V): Phosphuranylite. *Am. Mineral.* **1950**, *35*, 756−763.

(28) Hogarth, D. D.; Nuffield, E. W. Studies of radioactive compounds. 7. Phosphuranylite and dewindtite. *Am. Mineral.* **1954**, *39* (5−6), 444−447.

(29) Morris, D. E.; Allen, P. G.; Berg, J. M.; ChisholmBrause, C. J.; Conradson, S. D.; Donohoe, R. J.; Hess, N. J.; Musgrave, J. A.; Tait, C. D. Speciation of uranium in Fernald soils by molecular spectroscopic methods: Characterization of untreated soils. *Environ. Sci. Technol.* **1996**, *30* (7), 2322−2331.

(30) Murakami, T.; Sato, T.; Ohnuki, T.; Isobe, H. Field evidence for uranium nanocrystallization and its implications for uranium transport. *Chem. Geol.* **2005**, *221* (1−2), 117−126.

(31) Liu, C. X.; Zachara, J. M.; Qafoku, O.; McKinley, J. P.; Heald, S. M.; Wang, Z. M. Dissolution of uranyl microprecipitates in subsurface sediments at Hanford site, USA. *Geochim. Cosmochim. Acta* **2004**, *68* (22), 4519−4537.

J

dx.doi.org/10.1021/es4056559 | *Environ. Sci. Technol.* XXXX, XXX, XXX−XXX